3D Printing of Integrated Metallic Reactor Catalysts: Concept and Application

Pope, F.; Fowler, M.; Giesen, D.; Drangai, L.; Rothenberg, G.

DOI
10.1002/ceat.202400087

Publication date
2024

Document Version
Final published version

Published in
Chemical Engineering & Technology

Frances Pope[1]
Millie Fowler[1]
Daan Giesen[2]
Larissa Drangai[3]
Gadi Rothenberg[1,*]

3D Printing of Integrated Metallic Reactor Catalysts: Concept and Application

Selective laser melting can be used to create custom-made monolith reactor components with embedded microscale catalytic sites. Doping with noble metals (0.01–0.04 % of Pt, Ir, Ru, or Rh) gave clean incorporation of the active metal particles metals. Yet catalytic activity was low, due to distribution of the active particles between the surface and the bulk of the monolith. Switching to cobalt enabled doping in higher amounts (1.5–2.0 %) with corresponding increase in activity. Using borohydride hydrolysis as a test reaction, we showed that a combined stainless steel and cobalt monolith was active in both batch and continuous systems, for at least 48 h, albeit with some loss of active material. The advantages and limitations of this catalyst/reactor preparation method are discussed.

Keywords: Additive manufacturing, Borohydride, Catalyst design, Catalyst synthesis, Reactor design

Received: February 19, 2024; *revised:* March 08, 2024; *accepted:* March 11, 2024

DOI: 10.1002/ceat.202400087

Supporting Information available online

1 Introduction

At the end of the 20th century, large-scale additive manufacturing (3D printing) was viewed as science fiction. Today, two decades later, it has become a commercially available technology that offers tangible benefits in many areas thanks to its versatility and precise design capabilities. In chemical processes, 3D printing allows for creating catalyst supports with complex geometries, optimizing surface area and reactivity [1]. The technique gives precise control over material composition and physical properties [2–4]. In particular, 3D printing of metals offers synergistic advantages for chemistry and chemical engineering.

The cost-effectiveness of 3D printing is striking, with reductions in material wastage ranging from 50 to 90 % [5]. Powder-based printing techniques require neither preproduction nor tooling, saving money and materials [6]. One can, in principle, incorporate multiple materials within a single structure [7]. This has important implications in heterogeneous catalysis: Traditionally, the chemical reactor and the catalyst within it are considered two different domains. Reactor design and optimization is an engineering task, while the catalysts belong to the chemists' regime. But this distinction is blurring. Today's commercial metal 3D printers feature micrometer-scale resolution, allowing, in theory at least, the printing of specific metallic reactor parts with embedded catalytic active sites [8–13], 3D printing of such combined metallic catalysts and reactor components gives four important advantages [14–16].

1. **Unified Fabrication and Assembly**: Simultaneously printing both catalysts and reactor components ensures a consolidated and intricately interconnected structure, reducing assembly requirements, time, and costs.
2. **Thermal Management**: 3D-printed reactor parts can be designed for heat transfer efficiency, ensuring controlled temperature regimes.
3. **Material Integration**: The flexibility of 3D printing allows the integration of diverse materials, optimizing catalytic and mechanical/structural properties.
4. **Tailored Design for Reactions**: Customizing catalysts and reactor components allows tailored designs for specific chemical reactions.

Here we examine the possibilities for printing stainless steel reactor inserts using selective laser melting (SLM) of metallic powders, shown in Sch. 1 [17, 18]. We then repeat the process, incorporating micrometer-sized particles of catalytically active metals into the reactor "walls." The catalysts are tested in batch and continuous modes using the hydrolysis of alkali borohydrides as a benchmark reaction.

Alkali borohydrides (MBH_4) are hydrogen carriers that are stable salts at room temperature. To release the hydrogen, they

[1]Frances Pope https://orcid.org/0000-0002-6179-4903, Millie Fowler https://orcid.org/0009-0005-5813-0515, Prof. Dr. Gadi Rothenberg https://orcid.org/0000-0003-1286-4474 (g.rothenberg@uva.nl)
Van 't Hoff Institute for Molecular Sciences, University of Amsterdam, Science Park 904, 1098 XH Amsterdam, The Netherlands.
[2]Daan Giesen https://orcid.org/0009-0003-2802-1583
Technology centre FNWI, University of Amsterdam, Science Park 904, 1098 XH Amsterdam, The Netherlands.
[3]Larissa Drangai https://orcid.org/0009-0003-5684-8684
Austrian Centre of Competence for Tribology, AC2T research GmbH, Viktor-Kaplan-Straße 2, Wiener Neustadt, 2700, Austria.

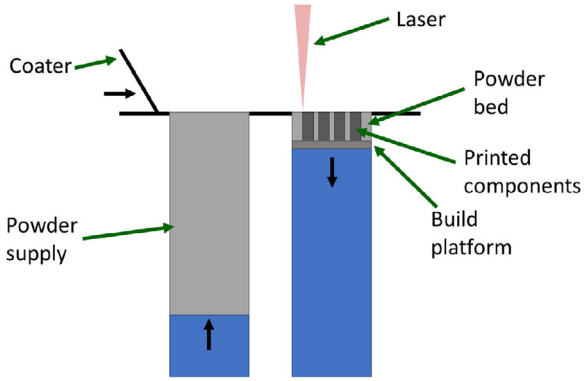

Scheme 1. Cross-section drawing of metal 3D printing by SLM. The black arrows show the movement of pieces within the printer (powder supply, printing powder bed, and the coater).

can be mixed with water. This is a spontaneous, albeit slow, reaction. The addition of a durable catalyst would make them suitable for real-world systems, particularly for on-demand hydrogen generation in portable applications [19–21]. The mass transfer requirements of these viscous solutions/mixtures and the fact that the reaction releases large amounts of gas make this system particularly suitable for testing combined catalyst/reactor setups.

2 Results and Discussion

2.1 Catalyst Synthesis by 3D Printing

First, we considered the chemical composition. We started with our support, stainless steel (alloyed powder), and our active metal site. In principle, SLM can be used for creating many alloys. We began by doping with small amounts of noble metals (Pt, Ir, Ru, or Rh). However, considering the size of the monoliths and the cost of the noble metals, we had to use very small amounts (0.01–0.04 wt%). The catalytic effects were minor, likely due to the statistical distribution of the active particles between the surface and the bulk of the structure (see details in the discussion, as well as in the Experimental Section and in the SI). We therefore switched to the more abundant Co, that allowed us to dope more of the active metal (1.5–2.0 wt%) into the monolith reactor insert.

The powders must meet some requirements dependent on the printing system used, particle shape, and size [22]. Ideally, the particles should be spherical [23]. This allows for an even melt to form under the laser of the printer and is less likely to result in defects and/or unwanted artifacts [24]. The particle size (and distribution) is dependent on what type of printing method is used [25, 26]. Our SLM system required a maximum particle size of 63 µm, and we found that particles <15 µm caused difficulties in printing and resulted in loss of structural integrity of the pieces. In particular, such small particles are more prone to causing defects by disturbing the melt pool (see SEM images in the SI) [27].

Second, we optimized the printer parameters, and particularly the laser, as listed in Tab. 1. Layer height, referring to the thickness of each powder layer, influences both mechanical and alloying properties [28]. Too thin a layer may cause insufficient powder deposition during recoating and/or undesirable melting of the underlying material. In contrast, too thick a layer may result in insufficient fusion with the underlying material and increase surface roughness. The melting should be done under inert atmosphere (N_2 or Ar), to prevent oxidation and fire hazard. Both the laser power and the scan speed affect the melt and thus the alloy composition and structure [29, 30]. All these parameters should be optimized based on your design and mechanical specifications.

Each parameter, chemical or mechanical, can be changed resulting in a unique catalyst printed to highly precise specification. Chemical composition can be controlled down to the micrometer level, and mechanical properties and geometry can be designed focused on the application at hand [32]. For example, designing a particular catalyst to control the flow of fluid through a system or a unique shape as an individual component within a pre-existing customized system [33].

Starting from our design as a CAD file, we preprocessed the 3D structure into layers (so-called "slices") in slicing software for toolpath generation (Sch. 2). Each of these slices describes the route that will be taken by the laser for that particular layer. Here we considered not only the desired geometry, but also the *contour exposure* versus *surface area exposure* of the laser. The two exposure types are important for both the design and structural integrity of the printed pieces. The SLM printer first carries out the *contour exposure*. Here the laser melting occurs along the outline (contour) of the structure, following a continuous path. Subsequently, the printer carries out the *surface area exposure*, running a hatch pattern over the larger bulk areas [34, 35].

The contour and surface exposures can be optimized to each following a different set of printing parameters (see Tab. 1). These optimizations are aimed at maximizing both the bulk properties (e.g., tensile strength, which depends on surface exposure parameters) and surface properties (e.g., roughness, which depends on contour exposure parameters). Typically, one changes the laser power and scan speed. The hatch distance parameter only applies to the surface area exposure. Optimizing this is important because surface area exposure can give a so-called full melt, yielding a smoother surface compared with contour exposure [36].

Table 1. List of printer parameters requiring consideration for SLM [31].

Property	Unit	Description
Laser power	W	Energy delivered by the laser to the powder bed. Usually considered alongside speed and spot size.
Laser speed	mm s^{-1}	Also known as scan speed, referring to the speed the laser passes over the powder bed.
Layer height	µm	Height of powder bed layer added from the powder supply.
Spot size	µm	Diameter of the laser beam at the powder bed.
Hatch distance	µm	Also known as scan spacing, it is the separation between successive laser beams in surface area exposure.
Atmosphere		An inert atmosphere of N_2 (or Ar) is used.

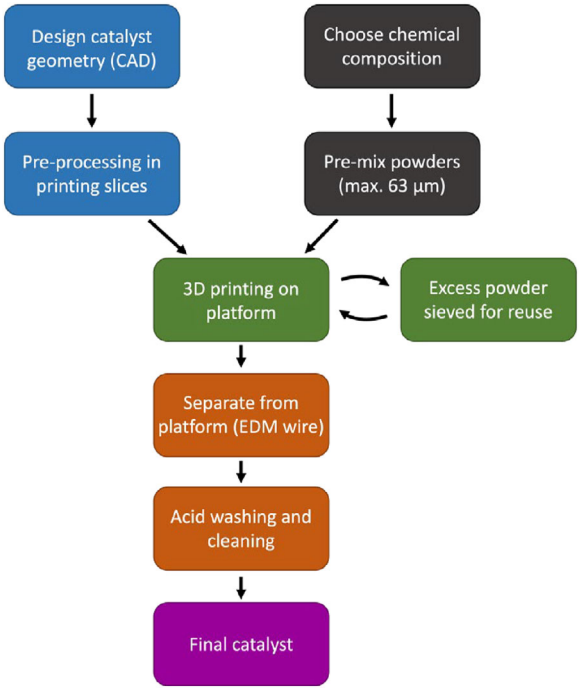

Scheme 2. Flow diagram showing the steps used in SLM-type 3D printing of metallic reactor/catalysts.

Once you have designed a model and have prepared your powder mixture, you can print your catalyst. Note that for SLM-type printing, an excess of powder is needed to fill the volume of your printing powder bed. With careful handling, this excess powder can be sieved and reused for further printing (see Sch. 2 above). This is an advantage for potential larger-scale operations. The objects are printed (welded) on a metallic printing platform. Once the print is complete, the structure is separated from the platform by Electric Discharge Machining using a brass wire. For catalysis applications, the final pieces should be washed to avoid any surface contamination from this step. Phosphoric acid solutions work well for this purpose (see Experimental Section for details).

Our design was aimed at tubular reactor inserts. The idea behind this design was to enable modularity and operational flexibility, by printing structured catalytic inserts that are easily added/removed to/from the reactor. Our reactor is a quartz tube, 80 mm long and 1.5 ± 0.1 mm thick, with an internal diameter of 13 mm. The printed inserts are cylinders, 10 mm high and 12 mm in diameter (Sch. 3). We prepared cylinders with three different internal channel geometries: small squares (1 mm), large squares (2 mm), small hexagons (1 mm across), and large hexagons (2 mm across). During the batch and flow experiments using KBH_4/KOH fuel solutions (see below), we found that the wider channels, either square or hexagonal, were needed for effective mass transfer.

2.2 Catalyst Characterization

Optical microscopy shows where the contour exposure has resulted in a well-defined melt at the structure's edge (Fig. 1a). We see a clear homogeneous melt that increases the structural integrity of the monolith. The surface is not completely smooth, as particles can be seen throughout the microscope image. However, these can be polished away if needed (for our application, this was not necessary). SEM imaging (Fig. 1b and 1c) clearly shows the distinction between contour and surface area exposure. You can see the surface area exposure hatch pattern followed by the melt pool.

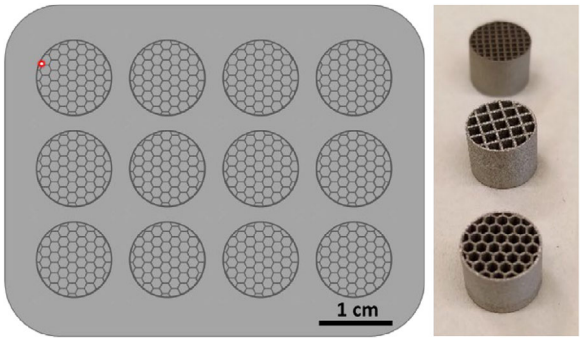

Scheme 3. (Left) Top view of manufacturing powder bed where the laser (shown as a red dot at the top left) moves across the surface forming a melt layer by layer and (right) photo of examples of three of the final catalyst monoliths (small square channels, large square channels, and large hexagonal channels).

EDX analysis confirmed the surface cobalt content to be within the expected range. This shows that the powder can be homogeneously mixed to reduce loss of catalytic material "hidden" in the bulk. These results were confirmed by ICP analysis (Tab. 2). Note that even with thorough mixing of the powder starting material before printing, the exposed surface area cannot guarantee the amount of exposed metal catalyst. However, this depends on the properties of the powder mixture and is not a fault of the 3D printing process itself.

In general, we expected the catalyst surface composition to follow that of the original powder. This was confirmed by X-ray photoelectron spectroscopy (XPS) analysis, which was run on thin 5 × 5 × 2 mm slices that were printed with the same composition and conditions as the reactor monoliths. The surface carbon content, however, was much higher than the theoretical value expected from the bulk composition. This could be caused by the high-temperature melting process, during which the smaller carbon atoms may segregate to the surface. The XPS analysis showed that the reactor/catalyst monoliths feature a combination of metallic cobalt (peak at 778 eV) and cobalt oxide (peaks at 780 and 783 eV, see Fig. 2). This corresponds to a thin layer of oxides on the metallic substrate, that likely forms during the SLM process.

SEM images of the cubic slices, as opposed to the monoliths, confirmed that the surface was not completely smooth for both 1.5 and 2.0 wt% Co pieces. In fact, you can see the roughness particularly from smaller particles within the melt (see Fig. 1 and SI). These small defect areas can provide a higher surface area for catalysis and help reach more of the active sites in the bulk [37].

We then tested the printed monolith catalysts using alkali borohydride hydrolysis as our benchmark reaction (Eq. 1). This reaction is a useful benchmark, especially when using

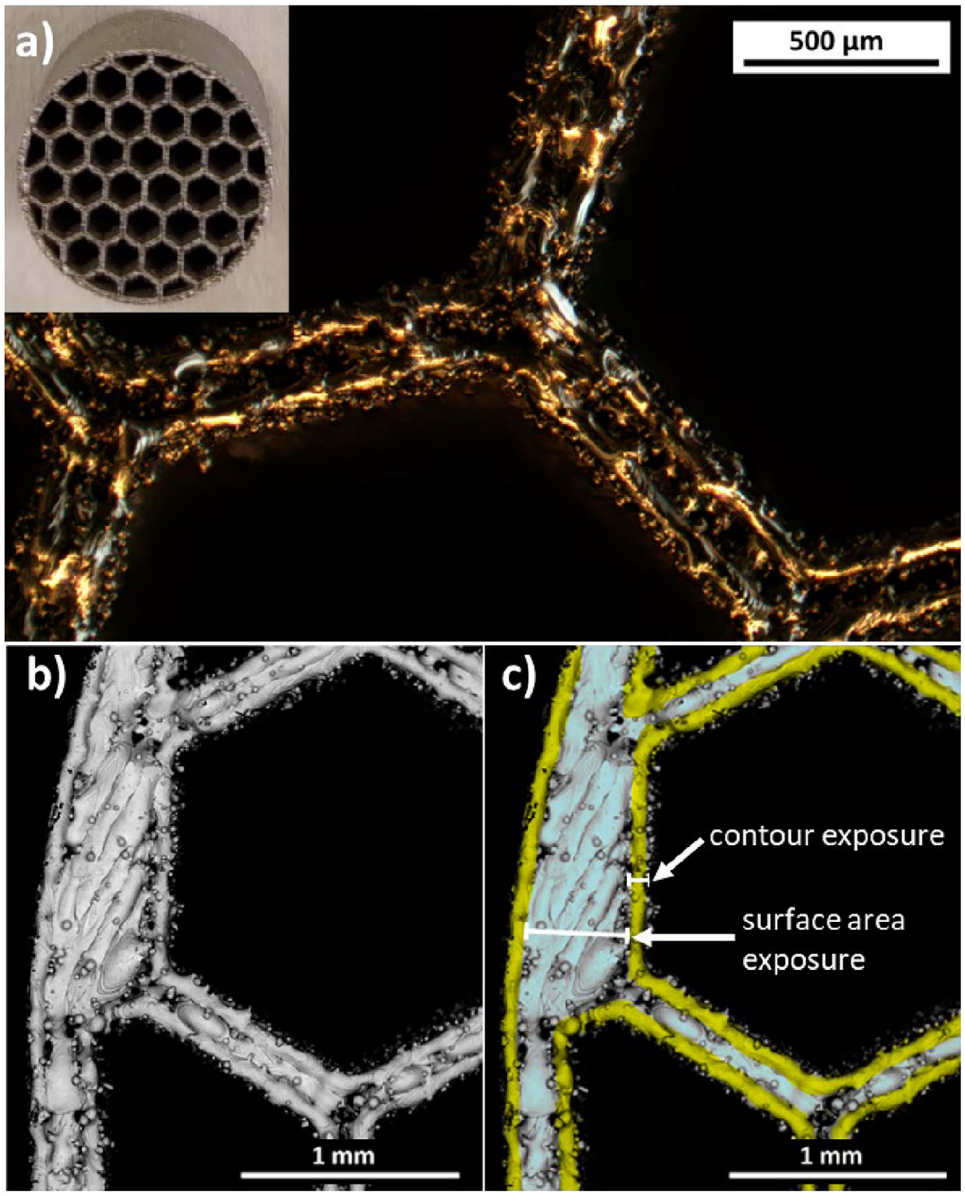

Figure 1. (a) Optical microscopy image of a Co-SS monolith with the large hexagonal channels at 50× magnification; the inset on the top left shows a regular photo of the same monolith. (b) and (c) SEM images at 35× magnification showing the *contour exposure* (yellow) and *surface area* exposure (cyan) within the monolith structure.

base-stabilized borohydride mixtures, as these give little or no product without a catalyst, but copious amounts of hydrogen when an active catalyst is present [38]. The reaction has more than pure academic interest, as borohydride salts are considered as viable candidates for hydrogen storage and release on industrial scale. $NaBH_4$ is most often used due to its a high hydrogen density of 10.7 wt% [39]. However, we opted for KBH_4 because the solubility of its corresponding metaborate salt, KBO_2, is significantly higher than that of $NaBO_2$ (1.51 and 0.28 g mL^{-1} at 25 °C, respectively) [40–42]. Using KBH_4 allows higher concentrations of the starting material and avoids problems caused by crystallization of the metaborate byproduct in real-life applications.

Table 2. Real bulk cobalt content of 1.5 and 5 wt% cobalt-stainless steel monoliths by ICP, EDX, and XPS.

	Cobalt content [wt%]	
Method	1.5	5
Expected bulk	1.5	5
ICP	1.42	4.31
EDX	1.34	5.39
XPS	1.29	4.08

Our hydrolysis mixture contained 5 % KBH_4 and 5 % KOH in 50 mL H_2O. This was heated to 65 °C before the adding the catalyst (see Experimental Section for details). The reaction gives four equivalents of hydrogen gas and a soluble metaborate byproduct, in a strongly basic solution (pH > 13).

$$KBH_4 + (2 + x)\,H_2O \rightarrow 4H_2 + KBO_2 \cdot xH_2O \quad (1)$$

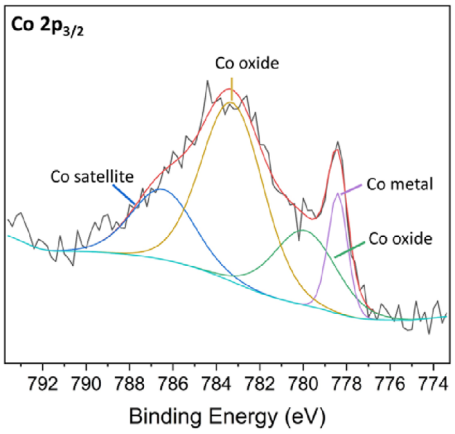

Figure 2. XPS analysis of the cobalt-containing samples. The fitting shows the presence of metallic cobalt and cobalt oxides (the ordinate shows the XP signal in arbitrary units).

As the catalytic reactor insert, we used a round monolith with 2 mm hexagonal channels (see Sch. 3). This structure allowed a continuous flow of the reactant solution throughout the experiment (using monoliths with channels of 1 mm created too much back pressure when used in the continuous reactor system). Each of the large-channel monoliths has a theoretical volume of 354 mm^3 and a nominal surface area of 2893 mm^2. The metallic monoliths are nonporous, with an average mass of 2.84 ± 0.02 g and a specific surface area of 10^{-3} m^2 gr^{-1}, way below that of any porous catalyst.

2.3 Catalyst Testing

The blank stainless steel supports showed no activity in the KBH_4 solution (Fig. 3; the small amount of H_2 generated is

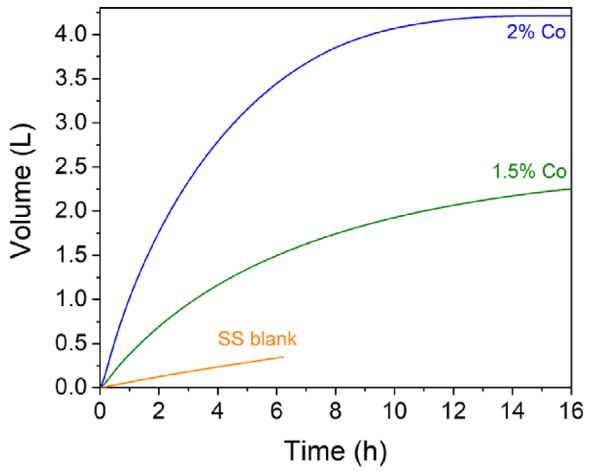

Figure 3. Comparison of hydrolysis of a blank SS support, 1.5 wt% Co/SS and 2.0 wt% Co/SS. The curves show the cumulative H_2 volume over time. Measurements were recorded using mass flow meters every second, giving highly precise curves with over 50,000 points (see Experimental Section for details). All results are averages of duplicate experiments.

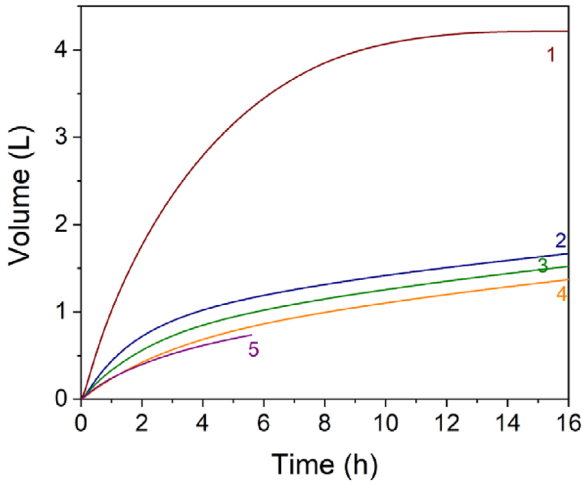

Figure 4. Multiple batch reactions using one 2.0 wt% Co/SS catalyst. 50 mL of solution (5 % KBH_4, 5 % KOH) was used at 65 °C. Measurements were taken every second by two mass flow meters in series. The catalyst was washed with water between runs to remove any potential metaborate byproduct build-up.

equivalent to the background spontaneous release of hydrogen, without any catalyst). Adding either 1.5 wt% Co/SS or 2.0 wt% Co/SS catalyst generated significant amounts of hydrogen, reaching, in the case of the 2.0 wt% sample, total theoretical volume of 4.1 L. As expected, the 1.5 wt% Co/SS catalyst was less active than the 2.0 wt% sample, though the difference in activity was not exactly proportional to the difference in Co content. We attribute this to the amount of exposed cobalt as opposed to the total cobalt content. Indeed, we expect that only the active particles that were part of the contour exposure would be exposed at the surface and available for catalysis. This is also the reason that doping very small amounts of noble metals gave only a minor advantage compared to the blank SS monolith (see SI, Fig. S7).

The catalyst was tested for its reusability. It was put in a 50 mL batch of fresh borohydride mixture back to back and washed with water after each run to reduce the risk of catalyst poisoning by the metaborate byproduct. This was done five times. Fig. 4 shows that there is a significant decrease in activity between runs 1 and 2. Further runs showed a smaller decrease in activity corresponding with the catalyst weight loss. In each case, when the catalyst was removed from the reaction mixture, the hydrolysis stopped. When the catalyst was weighed between runs, however, we saw some weight loss due to mechanical damage (see details in SI). This was particularly significant between runs 1 and 2, corresponding to the drop in catalytic activity. This weight loss is likely caused by vigorous formation of hydrogen bubbles at the surface, wherein microbubbles of hydrogen gas can cause cracking of the cobalt catalyst particles.

We also tested the continuous performance of the catalyst in a flow reactor (details of the reactor system and its construction are given elsewhere [43]). The same reaction mixture (5 % KBH_4, 5 % KOH in H_2O) was pumped through the catalytic monolith containing 5 wt% Co/SS at a rate of 0.8 mL min^{-1}. The rate of reaction was analyzed over 48 h. As shown in Fig. 5, the reaction rate decreases slightly over time, yet the monolith retained >99 % of its mass after 48 h.

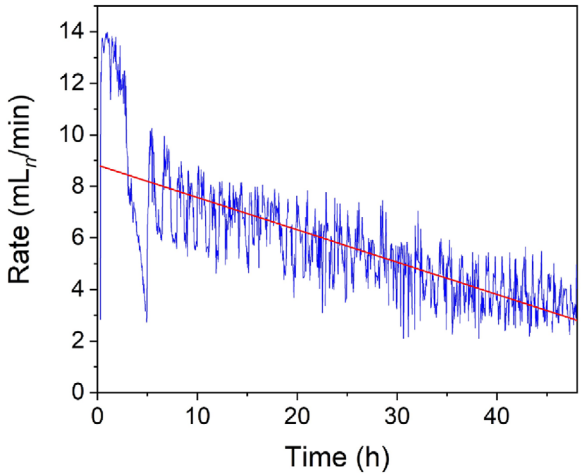

Figure 5. Hydrogen generation rate using a single monolith containing 5.0 wt% Co/SS in a continuous reactor over 48 h. Gas flow was measured by two mass flow meters in series, measuring the rate of H_2 every second. Note that in this continuous system, the hot hydrogen product stream is passed through a bubbler to remove water vapor. This causes systemic rate fluctuations due to the pressure build-up required of the gas to pass through the bubbler. These fluctuations (≈100 data points) are an artefact and have been removed, still leaving >170,000 data points. Of these, only 1000 points are shown here for clarity (the full data set is included in the SI).

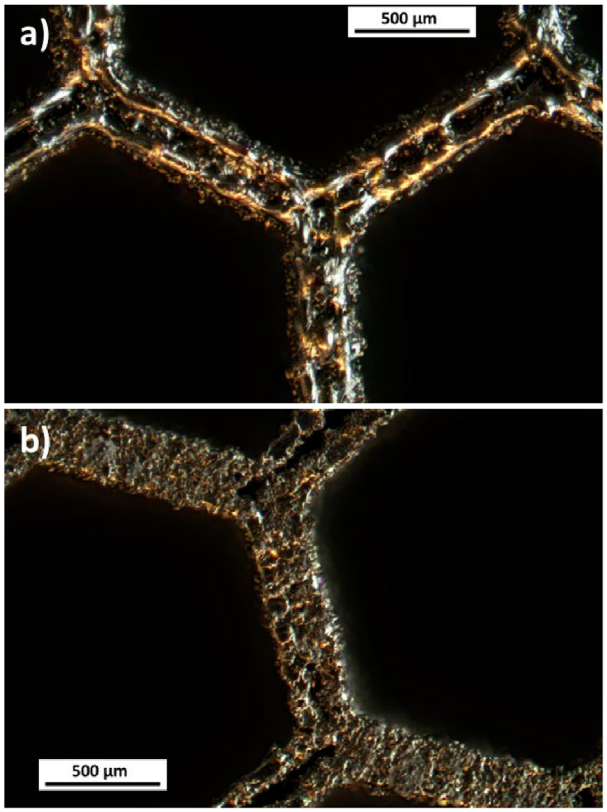

Figure 6. Optical microscope images at 50× magnification after hydrolysis. a) Sample that does not appear to suffer significant damage under harsh reaction conditions. b) Sample that lost density due to the harsh reaction conditions.

Postreaction characterization of the monoliths showed an increase in surface roughness. This could reflect some leaching or flaking off of surface species as a result of the high OH^- concentration and/or the vigorous formation of hydrogen gas bubbles. However, this increase in roughness differed across samples. Fig. 6 shows photos of two samples with the same metal content that underwent the same reaction conditions. One sample was unaffected (top) whereas the other shows increased surface roughness and a slightly lower density (bottom). XPS did not show a significant chemical difference before and after the reaction. This confirms that chemical poisoning by the metaborate side product did not occur.

Both the reusability tests and exposure in a continuous reaction show that mass loss of the catalysts correlates to a reduction in activity over time. This mass loss was significantly lower in the continuous system compared to the multiple batch reactions. Changes in 3D printing parameters, chemical composition, or postprinting processing, such as annealing, could help tackle this issue. The final printing recipe would depend on the application at hand. However, the continued activity in the corrosive environment of our liquid–gas benchmark systems shows that 3D printing of metallic reactor/catalyst components is an effective method for designing and producing tailor-made systems.

3 Conclusion

3D printing of metallic reactor parts starting from powder mixtures is a powerful tool for preparing integrated reactor/catalyst components. The method's simplicity and versatility allow for designing tailor-made reactor parts, wherein metal catalyst microparticles are embedded within the bulk structures. The process is scalable and reproducible. Moreover, the length scales and resolution accessible by commercially available SLM printers are within the range needed for real-life reactors. The resulting reactor catalyst parts are prone to surface leaching and active site inhibition just like traditional supported catalysts. Yet there are important differences: the SLM 3D printing of (multi)metallics integrates the catalyst particles directly into the structure. As such, they are more like doped crystals than simple supported catalysts. One advantage of this method is the possibility for including reactor mass- and heat-transfer considerations at the catalyst synthesis stage (and vice versa). A disadvantage of this approach is that there is (currently) no method for guaranteeing that the active particle would actually be available on the surface and not completely embedded in the "walls" of the monolith tunnels. Yet another limitation is that these laser-welded monoliths are nonporous, so their surface area is very low. That said, we foresee a steep learning curve in the optimization of making such combined reactors/catalysts, with corresponding benefits. We hope that these results will encourage other scientists to consider printing and using combined metal reactor catalysts.

Table 3. Parameters of the 3D printer used for the synthesis of the catalysts.

Parameter	Value
Laser power (surface area exposure)	90 W
Laser power (contour exposure)	60 W
Laser speed (surface area exposure)	600 mm s^{-1}
Laser speed (contour exposure)	450 mm s^{-1}
Layer height	25 µm
Spot size	50 µm
Hatch distance	83 µm
Max. particle size of powder	63 µm
Atmosphere	N_2 (O_2 < 0.3 %)

4 Experimental Section

4.1 Materials and Instrumentation

Unless stated otherwise, all chemicals were purchased from commercial sources and used as received. Stainless steel (316L, 63 µm, exact composition in SI) was purchased from AP&C (a GE additive company) and cobalt powder (45 µm) was bought from Sigma Aldrich. CAD files were preprocessed into slices using Autodesk Netfabb for toolpath generation and the 3D printer used was a Concept Laser Mlab R printer (fiber laser) using SLM technique. The pieces were cut from the printing plate using a Sodick SLC400 G with a brass electrode wire of 250 µm (Megacut Plus Ø 0.25 mm) and the "coarse" cutting parameter. Optical microscopy images were taken using a Delphin-X Observer with a sCMEX-20 camera and processed with ImageFocusAlpha software. Hydrogen generation was measured by two Bronkhorst EL-Flow Prestige mass flow meters in series (200 mL_n min^{-1} and 2 L_n min^{-1}) and the rate collected every second by Bronkhorst Flowsuite software. All data was further processed in Origin 2018. ICP–OES was measured using an Agilent 5800 VDV Spectrometer. 3D laser microscope images were captured using a Keyence VK-X1100 3D Laser Confocal Microscope at 50× magnification. SEM–EDS was performed using a Hitachi TM3000 Tabletop SEM paired with a Bruker Quantax 70. XPS measurements were taken on a ThermoFischer Scientific Thetaprobe with a monochromatic Al Kα X-ray source (1486.6 eV). A 0.2 eV energy step was used. Peak fittings were done using Gaussian/Lorentzian curve fittings on ThermoFischer Scientific Avantage Data System software.

4.2 General Procedure for Catalyst Synthesis/3D Printing

500 g powder mix of stainless steel and the desired cobalt power were mixed and transferred to the powder supply unit of the 3D printer. The CAD file was translated into printing slices and these were uploaded to the printer together with the printer and laser parameters input (see Tab. 3). Six pieces were printed in a batch onto a stainless steel build platform. The samples were sliced off from the printing plate with a brass wire and washed with a 10 % H_3PO_4 soln to remove any brass contamination. They were then washed with water before being left to dry in air.

4.3 Catalyst Synthesis Example: 5 wt% Co with Stainless Steel

500 g powder batch for the 3D printer was prepared. 25 g of cobalt powder (max. 45 µm) was added to 475 g of stainless steel powder (max. 63 µm). The powder was mixed and then transferred to the powder supply of the 3D printer. The final monoliths were sliced from the stainless steel platform with a brass wire and washed first with 10 % H_3PO_4 soln and then water and left to dry overnight in air.

4.4 Hydrogen Generation (Batch Reaction)

All batch reactions were performed at 65 °C and stirred at 250 rpm. KOH (5 %, 2.5 g, 45 mmol, 0.89 M) was added to H_2O and preheated to 65 °C. KBH_4 (5 wt%, 2.5 g, 46 mmol), a monolith, and a stir bar were placed in a round-bottom flask with three necks. One neck was sealed with a septum, one with a dropping funnel, and one connected to a cold trap. The RBF was warmed to 65 °C in an oil bath. The preheated KOH solution was added to the dropping funnel and the entire system was flushed with air. The KOH soln was dropped into the RBF and the H_2 flow rate was measured by mass flow meters.

4.5 Hydrogen Generation (Continuous Reactor)

All continuous reactions were performed at 65 °C. KOH (5 wt%, 0.89 M) was dissolved in H_2O at room temperature. Then KBH_4 (5 wt%) was added to the solution. This was connected to the continuous reactor where one monolith was placed. The solution was pumped through the continuous reactor and heated to 65 °C in the system by the oven containing the reactor and monolith. The solution was pumped using a liquid pump at 0.8 mL min^{-1}. All gases were passed through a bubbler before passing through the mass flow meters.

4.6 ICP Analysis

ICP samples were placed in 4 mL Aqua Regia (HNO_3:HCl of 1:3) for 24 h until fully dissolved. They were then diluted with H_2O by factors of 2,000 and 20,000. For high-concentration elements, radial view of plasma was used. For low-concentration elements, axial view of the plasma was used.

Supporting Information

Supporting Information for this article can be found under DOI: https://doi.org/10.1002/ceat.202400087.

Acknowledgments

We thank Dr. C. Tomastik for running the XPS and SEM–EDX measurements, J. Brenner for discussion on the XPS results, N. Gofman for designing the monolith STL files, and P. Kolpakov for help with the SEM measurements. This work was funded by the "Austrian COMET-Program" (project InTribology1, no. 872176) via the Austrian Research Promotion Agency (FFG) and the federal states of Niederösterreich and Vorarlberg and has been carried out within the "Excellence Centre of Tribology" (AC2T research GmbH).

Abbreviations

EDX	energy-dispersive x-ray
ICP	inductively coupled plasma spectroscopy (coupled with OES)
OES	optical emission spectroscopy
RBF	round bottom flask
SEM	scanning electron microscopy
SS	Stainless steel

References

[1] Q. Wei, H. Li, G. Liu, Y. He, Y. Wang, Y. E. Tan, D. Wang, X. Peng, G. Yang, N. Tsubaki, *Nat. Commun.* **2020**, *11*, 4098.
[2] X. Li, F. Rezaei, A. A. Rownaghi, *Microporous Mesoporous Mater.* **2019**, *276*, 1–12.
[3] X. Zhou, C. Liu, *Catal. Today* **2020**, *347*, 2–9.
[4] J. S. Manzano, H. Wang, L. Qi, I. I. Slowing, *Appl. Catal., A* **2020**, *605*, 117794.
[5] C. Hurt, M. Brandt, S. S. Priya, T. Bhatelia, J. Patel, P. Selvakannan, S. Bhargava, *Catal. Sci. Technol.* **2017**, *7*, 3421–3439.
[6] E. Sachs, M. Cima, J. Cornie, D. Brancazio, J. Bredt, A. Curodeau, T. Fan, S. Khanuja, A. Lauder, J. Lee, S. Michaels, *CIRP Ann. Manuf. Technol.* **1993**, *42*, 257–260.
[7] M. Attaran, *Bus. Horiz.* **2017**, *60*, 677–688.
[8] O. H. Laguna, P. F. Lietor, F. J. I. Godino, F. A. Corpas-Iglesias, *Mater. Des.* **2021**, *208*, 109927.
[9] E. Bogdan, P. Michorczyk, *Materials* **2020**, *13*, 4534.
[10] L. Chen, S. Zhou, M. Li, F. Mo, S. Yu, J. Wei, *Catalysts* **2022**, *12*, 1081.
[11] C. Parra-Cabrera, C. Achille, S. Kuhn, R. Ameloot, *Chem. Soc. Rev.* **2018**, *47*, 209–230.
[12] A. Bandyopadhyay, B. Heer, *Mater. Sci. Eng.: R: Rep.* **2018**, *129*, 1–16.
[13] B. Nagarajan, Z. Hu, X. Song, W. Zhai, J. Wei, *Engineering* **2019**, *5*, 702–720.
[14] D. Flagiello, D. Tammaro, A. Erto, P. L. Maffettone, A. Lancia, F. Di Natale, *Chem. Eng. Sci.* **2022**, *260*, 117853.
[15] L. Chatre, J. Socci, S. J. Adams, P. Denissenko, N. Cherkasov, *Chem. Eng. J.* **2021**, *420*, 129762.
[16] J. Wu, Y. Yan, L. Zhang, Z. Qin, S. Tao, *Adv. Mater. Technol.* **2019**, *4*, 1800515.
[17] N. T. Aboulkhair, M. Simonelli, L. Parry, I. Ashcroft, C. Tuck, R. Hague, *Prog. Mater. Sci.* **2019**, *106*, 100578.
[18] T. D. Ngo, A. Kashani, G. Imbalzano, K. T. Q. Nguyen, D. Hui, *Composites, Part B* **2018**, *143*, 172–196.
[19] V. I. Simagina, A. M. Ozerova, O. V. Komova, O. V. Netskina, *Catalysts* **2021**, *11*, 268.
[20] Y. Chen, H. Kim, *Energy* **2010**, *35*, 960–963.
[21] H. X. Nunes, M. J. F. Ferreira, C. M. Rangel, A. M. F. R. Pinto, *Int. J. Hydrogen Energy* **2016**, *41*, 15426–15432.
[22] D. Bourell, J. P. Kruth, M. Leu, G. Levy, D. Rosen, A. M. Beese, A. Clare, *CIRP Ann. Manuf. Technol.* **2017**, *66*, 659–681.
[23] J. A. Slotwinski, E. J. Garboczi, *JOM* **2015**, *67*, 538–543.
[24] C. L. A. Leung, S. Marussi, R. C. Atwood, M. Towrie, P. J. Withers, P. D. Lee, *Nat. Commun.* **2018**, *9*, 1355.
[25] C. Meier, R. Weissbach, J. Weinberg, W. A. Wall, A. J. Hart, *J. Mater. Process. Technol.* **2019**, *266*, 484–501.
[26] Y. Bai, G. Wagner, C. B. Williams, *J. Manuf. Sci. Eng.* **2017**, *139*, 081019. DOI: https://doi.org/10.1115/1.4036640.
[27] B. Zhang, Y. Li, Q. Bai, *Chin. J. Mech. Eng.* **2017**, *30*, 515–527.
[28] L. E. Murr, *Metallogr. Microstruct. Anal.* **2018**, *7*, 103–132.
[29] S. Ghouse, S. Babu, R. J. Van Arkel, K. Nai, P. A. Hooper, J. R. T. Jeffers, *Mater. Des.* **2017**, *131*, 498–508.
[30] J. Kluczyński, L. Śnieżek, K. Grzelak, J. Mierzyński, *Materials* **2018**, *11*, 2304.
[31] S. Kumar, in *Comprehensive Materials Processing* (Eds: S. Hashmi, G. F. Batalha, C. J. Van Tyne, B. Yilbas), Elsevier, Oxford, **2014**, pp. 93–134.
[32] M. K. Thompson, G. Moroni, T. Vaneker, G. Fadel, R. I. Campbell, I. Gibson, A. Bernard, J. Schulz, P. Graf, B. Ahuja, F. Martina, *CIRP Ann.* **2016**, *65*, 737–760.
[33] D. Rodriguez-Padron, A. Ahmad, P. Romero-Carrillo, R. Luque, R. Esposito, *Trends Chem.* **2022**, *4*, 739–753.
[34] P. Wüst, A. Edelmann, R. Hellmann, *Materials* **2020**, *13*, 418.
[35] D. Pitassi, E. Savoia, V. Fontanari, A. Molinari, V. Luchin, G. Zappini, M. Benedetti, D. Pitassi, E. Savoia, V. Fontanari, A. Molinari, V. Luchin, G. Zappini, M. Benedetti, in *Finite Element Method - Simulation, Numerical Analysis and Solution Techniques*, IntechOpen, London **2017**.
[36] E. Abele, M. Kniepkamp, *Surf. Topogr. Metrol. Prop.* **2015**, *3*, 034007.
[37] A. Sola, A. Nouri, *J. Adv. Manuf. Process* **2019**, *1*, e10021.
[38] F. Pope, N. I. Watson, A. Deblais, G. Rothenberg, *ChemPhysChem* **2022**, *23*, e202200428.
[39] L. Laversenne, C. Goutaudier, R. Chiriac, C. Sigala, B. Bonnetot, *J. Therm. Anal. Calorim.* **2008**, *94*, 785–790.
[40] N. P. Nies, R. W. Hulbert, *J. Chem. Eng. Data* **1967**, *12*, 303–313.
[41] O. Krol, J. Andrieux, J. J. Counioux, R. Tenu, C. Goutaudier, in *XXXV JEEP –35th Conference on Phase Equilibria*, EDP Sciences, Annecy, France **2009**, p. 00023.
[42] P. Toledano, *Compt. Rend. Acad. Sci.* **1962**, *254*, 2348–2350.
[43] F. Pope, J. Jonk, M. Fowler, P. C. M. Laan, N. J. Geels, L. Drangai, V. Gitis, G. Rothenberg, *Green Chem.* **2023**, *25*, 5727–5734.

